



THE INTERPRETATION OF THE MULTI-WAVELENGTH AFTERGLOW EMISSION OF SHORT GRB 140903A

SHUAI ZHANG^{1,2}, ZHI-PING JIN¹, YUAN-ZHU WANG^{1,2}, AND DA-MING WEI¹¹ Key Laboratory of Dark Matter and Space Astronomy, Purple Mountain Observatory, Chinese Academy of Sciences, Nanjing, 210008, China;

jin@pmo.ac.cn, dmwei@pmo.ac.cn

² University of Chinese Academy of Sciences, Yuquan Road 19, Beijing, 100049, China

Received 2016 August 27; revised 2016 November 15; accepted 2016 December 2; published 2017 January 19

ABSTRACT

GRB 140903A, a short duration γ -ray burst (SGRB) detected by *Swift*, is characterized by its long-lasting radio emission among SGRBs. In addition to the $\sim 10^6$ s radio afterglow emission, the afterglow of GRB 140903A displays a plateau from 10^3 s to 7×10^3 s in the X-rays. In this work, we attribute the X-ray plateau to the energy injection into the decelerating blast wave and then model the later radio/optical/X-ray afterglow emission within the standard fireball afterglow model. The afterglow emission has been well reproduced with reasonable physical parameters, including a jet half-opening angle of ~ 0.05 .

Key words: gamma-ray burst: general – gamma-ray burst: individual (GRB 140903) – ISM: jets and outflows

1. INTRODUCTION

Gamma-ray bursts (GRBs) are the most energetic flashes of soft γ -ray from the deep universe. Based on their duration distribution, GRBs can be generally divided into two groups, including the so-called short GRBs (SGRBs; the duration is shorter than 2 s) and long GRBs. (Kouveliotou et al. 1993). Usually the long GRBs are associated with bright supernovae and thus should be from massive star collapse (Woosley & Bloom 2006). The SGRBs, however, are expected to be from neutron star mergers (including both the double neutron star mergers and neutron star–black hole mergers; Eichler et al. 1989). The compact object merger origin of SGRBs has been strongly supported by their afterglow and host galaxy observations (Berger 2014; Fong et al. 2015) and the identification of Li-Paczynski macronovae (Li & Paczyński 1998; Kasen et al. 2013) in SGRB 130603B (Berger et al. 2013; Tanvir et al. 2013), long-short GRB 060614 (Jin et al. 2015; Yang et al. 2015) and SGRB 050709 (Jin et al. 2016). SGRBs are hence widely believed to be promising gravitational wave (GW) sources and important sites of generating heavy elements (Eichler et al. 1989; Jin et al. 2016) and the SGRB/GW association is expected to be reliably established in the advanced LIGO/Virgo era (see Li et al. 2016 and the references therein). The observations of SGRBs have attracted wider and wider attention and the modeling of the afterglow can provide additional information. For instance, the derivation of the half-opening angle of the SGRB ejecta is important for estimating the detection prospect of GW emission from neutron star mergers by the advanced LIGO/Virgo network (Berger 2014), and the afterglow modeling may reveal the nature of the central engine of short GRBs.

In this work, we focus on GRB 140903A, a short burst characterized by its long-lasting radio emission. Before the detection of this event, there had been just three short GRBs with radio afterglow and all had been detected by The Jansky Very Large Array (VLA), including GRB 050724A (Berger et al. 2005; Panaitescu 2006), GRB 051221A (Soderberg et al. 2006), and GRB 130603B (Fong et al. 2014). Among the limited sample, GRB 140903A has the longest radio afterglow detection ($\sim 10^6$ s). In addition to the long-lasting radio afterglow emission, the afterglow of GRB 140903A

displays a plateau from 10^3 s to 7×10^3 s in the X-rays. The main purpose of this work is to interpret these features. We also carry out a statistical study to examine why the radio afterglow detection of SGRBs is so rare.

Recently, Troja et al. (2016) reported their observing result of GRB 140903A. They monitored the X-ray afterglow for up to 15 days with *Chandra*. Together with the optical and radio afterglow data, they found an achromatic jet break about one day after the burst. They discussed the nature of the GRB progenitor system and concluded that this event likely originated from a compact binary merger. An off-axis jet model was used to interpret the multi-band afterglow. In this work, we carry out an independent analysis in the on-axis jet scenario.

2. THE AFTERGLOW EMISSION OF SGRB 140903A AND THE INTERPRETATION

2.1. The Afterglow Data

At 15:00:30 UT on 2014 October 03, GRB 140903A triggered the Burst Alert Telescope (BAT) on board the *Swift* satellite (Cummings et al. 2014). Its duration T_{90} (15–350 keV) is 0.30 ± 0.03 s. The time-averaged spectrum between $T_0 - 0.01$ to $T_0 + 0.35$ s is best fitted by a simple power-law model, with a photon index of 1.99 ± 0.12 (Palmer et al. 2014).

Swift XRT began to observe the position of GRB 140903A at about 59 s after the BAT trigger (Kennea & Cummings 2014) and detected the afterglow (De Pasquale et al. 2014). The X-ray afterglow decay first ($\alpha \sim 0.2$) before 1000 s and then followed by a plateau with a flux $\sim 10^{-11}$ erg cm $^{-2}$ s $^{-1}$ until about 10^4 s and then turned to a more rapid decay (De Pasquale et al. 2014; Troja et al. 2016). *Chandra* took two epochs of observations of the afterglow at about 3 and 21 days after the burst and both detected the source (Sakamoto et al. 2014; Troja et al. 2016). Comparing them with the *Swift* XRT data, there was a jet break at about one day (Troja et al. 2016).

The afterglow of GRB 140903 had been observed by many ground-based telescopes. Among them, the 4.3 m Discovery Channel Telescope (Capone et al. 2014), the robotic Palomar 60 inch telescope (Cenko & Perley 2014), the Gemini-North telescope (Cucchiara et al. 2014; Levan et al. 2014), the Pan

STARRS survey telescope (Fruchter 2014), the Faulkes Telescope North (Dichiara et al. 2014), and the Nordic Optical Telescope (Xu et al. 2014) all detected the optical counterpart of the X-ray afterglow. Gemini GMOS observed the source in spectroscopic mode at about 14.6 hr after the burst, and the redshift $z = 0.351$ was determined by identifying the H β and O III emission lines and the Na I absorption line (Cucchiara et al. 2014). This was confirmed by later spectroscopy of the host galaxy by GTC, which detected a H α line at the same redshift (Troja et al. 2016). The radio afterglow of 6.1 GHz and 9.8 GHz was also detected by the VLA at about 10 hr after the trigger of BAT (Fong 2014), it was still detectable until 10^6 s. The radio flux rises first and then decays, the peak flux density is $\sim 200 \mu\text{Jy}$ at about 2×10^5 s (Troja et al. 2016). The Giant Metrewave Radio Telescope also detected the radio emission (Nayana & Poonam 2014). In this work, we give an interpretation of these observational features within the framework of external forward shock model with energy injection.

2.2. X-Ray Afterglow Flat Segment Due to the Energy Injection

A flat segment of X-ray afterglow has been detected in a good fraction of long GRB afterglows (Nousek et al. 2006; Zhang et al. 2006) and some SGRB afterglows (Burrows et al. 2006). Such a phenomena has been widely interpreted as the energy injection from the prolonged activity of the central engine (Fan & Xu 2006; Zhang et al. 2006). However, sometimes the optical afterglow emission cannot be interpreted self-consistently within such a scenario (Fan & Piran 2006; Panaitescu et al. 2006; Liang et al. 2007).

The energy injection can be written generally as (Cohen & Piran 1999; Zhang & Mészáros 2001; Zhang et al. 2006)

$$\frac{dE}{dt} = A(1+z)^{-1} \left(\frac{t}{t_0} \right)^{-q}, \quad t_i < t < t_f \quad (1)$$

where t_i and t_f represent the start and end time of energy injection. At the time of t_c (when the amount of injected energy equals the initial kinetic energy in the outflow) the dynamical evolution of the GRB ejecta is changed significantly, i.e., $\int_{t_i}^{t_c} (dE/dt) dt \sim E_k$, where E_k is the kinetic energy of the outflow. Then we get $At_0^q(t_c^{1-q} - t_i^{1-q}) \sim (1+z)(1-q)E_k$.

From the observations, we know that $\nu_c(t_d = 1) \gtrsim 10$ keV for SGRB 140903A. In this case, the X-ray flat plateau declines as $\alpha = \frac{(2p-4) + (p+2)q}{4}$ (Zhang et al. 2006). For a typical value of $p \sim 2.2 - 2.5$, the X-ray flat segment of SGRB 140903A is in agreement with the case of $q \sim 0$, i.e., the central engine is a pulsar-like compact object. Similar conclusions have been drawn, for example, for SGRB 151221A (Fan & Xu 2006). In the case of long GRBs, please see Dai & Lu (1998) and Zhang & Mészáros (2001). For $q \sim 0$, we have $A \sim \frac{(1+z)E_k}{t_c - t_i}$.

We consider the energy injection (Pacini 1967; Gunn & Ostriker 1969) as

$$\frac{dE}{dt} \approx \frac{6.2 \times 10^{47}}{1+z} \text{ erg s}^{-1} B_{\perp,14}^2 R_{s,6}^6 \Omega_4^4 \left[1 + \frac{t}{(1+z)T_0} \right]^{-2}, \quad (2)$$

where B_{\perp} and R_s are the components of the dipole magnetic field strength perpendicular to the rotation axis and radius of the magnetar, respectively, and Ω is the initial angular frequency of rotation. The initial spin-down timescale in the

rest frame is

$$T_0 \approx 1.6 \times 10^5 \text{ s } B_{\perp,14}^{-2} \Omega_4^{-2} I_{45} R_{s,6}^{-6} \quad (3)$$

in which $I \sim 10^{45}$ is the typical moment of inertia of magnetar. Here and after, we adopted the convention $Q_x = Q/10^x$ in cgs units.

When $t \ll (1+z)T_0$, the energy injection rate is a constant, so with our magnetar model one requires $q \sim 0$ for $t_c < (1+z)T_0$, we can derive

$$A \sim \frac{(1+z)E_k}{t_c - t_i} \sim 6.2 \times 10^{47} \text{ erg s}^{-1} B_{\perp,14}^2 R_{s,6}^6 \Omega_4^4. \quad (4)$$

For $t > (1+z)T_0$, the energy injection rate drops rapidly. So we have

$$t_f \sim (1+z)T_0 \sim 1.6 \times 10^5 \text{ s } (1+z) B_{\perp,14}^{-2} \Omega_4^{-2} I_{45} R_{s,6}^{-6}. \quad (5)$$

The total energy injection can be estimated as $E_{\text{inj}} = AT_0$, so together with (3) and (4) we can get $E_{\text{inj}} = t_f E_k / (t_c - t_i) \sim 10^{53} \text{ erg } I_{45} \Omega_4^2$. Then the ratio of total injected energy to initial kinetic energy is

$$\frac{E_{\text{inj}}}{E_k} \sim \frac{10^{53} \text{ erg } I_{45} \Omega_4^2}{E_k}. \quad (6)$$

From the X-ray afterglow of GRB 140903A, we can infer that the energy injection begins at about 1000 \sim 2000 s and ends at about 7000 s, so we estimate $t_c - t_i \sim 1000$ s and $t_f \sim 7000$ s. Thus $E_{\text{inj}}/E_k \sim t_f/(t_c - t_i) \sim 7$. Substituting this into Equation (6), we get $E_k \sim 1.4 \times 10^{52} \text{ erg } I_{45} \Omega_4^2$. Then, through Equation (4), we obtain $A \sim 1.9 \times 10^{49} \text{ erg } I_{45} \Omega_4^2$, here $z = 0.351$ is adopted. By assuming typical values of $I_{45} = 1$ and $\Omega_4 = 0.58$ (Shapiro & Teukolsky 1983, p. 663), we can estimate $E_k \sim 4.7 \times 10^{51} \text{ erg}$ and $A \sim 6.4 \times 10^{48} \text{ erg s}^{-1}$.

We can also constrain the ellipticity $\epsilon \equiv \frac{a-b}{(a+b)/2}$ of the magnetar if we assume that gravitational wave radiation is not important. The spin-down timescale of gravitational wave radiation can be estimated as $\tau_{\text{gw}} \sim 3 \times 10^{-3} \epsilon^{-2} I_{45}^{-1} \Omega_4^{-4} \text{ s}$ (Shapiro & Teukolsky 1983, p. 663). From $\tau_{\text{gw}} > t_f \sim 7000$ s, we can get $\epsilon < 6.5 \times 10^{-4} I_{45}^{-1/2} \Omega_4^{-2}$.

2.3. Analytical Estimate of Forward Shock Physical Parameters

The forward shock emission from GRB outflow can be parameterized as (e.g., Piran 1999; Yost et al. 2003; Fan & Piran 2006)

$$F_{\nu, \text{max}} = 6.6 \text{ mJy} \left(\frac{1+z}{2} \right) D_{L,28.34}^{-2} \epsilon_{B,-2}^{1/2} E_{k,53} n_0^{1/2}, \quad (7)$$

$$\nu_m = 2.4 \times 10^{16} \text{ Hz } E_{k,53}^{1/2} \epsilon_{B,-2}^{1/2} \epsilon_{e,-1}^2 C_p^2 \left(\frac{1+z}{2} \right)^{1/2} t_{d,-3}^{-3/2}, \quad (8)$$

$$\nu_c = 4.4 \times 10^{16} \text{ Hz } E_{k,53}^{-1/2} \epsilon_{B,-2}^{-3/2} n_0^{-1} \times \left(\frac{1+z}{2} \right)^{-1/2} t_{d,-3}^{-1/2} \frac{1}{(1+Y)^2}, \quad (9)$$

where $C_p \equiv 13(p-2)/[3(p-1)]$, ϵ_e (ϵ_B) is the fraction of energy of shocked electrons (magnetic field), the Compton parameter $Y \sim (-1 + \sqrt{1 + 4\eta\epsilon_e/\epsilon_B})/2$, $\eta \sim \min\{1, (\nu_m/\bar{\nu}_c)^{(p-2)/2}\}$, and $\bar{\nu}_c = (1+Y)^2 \nu_c$.

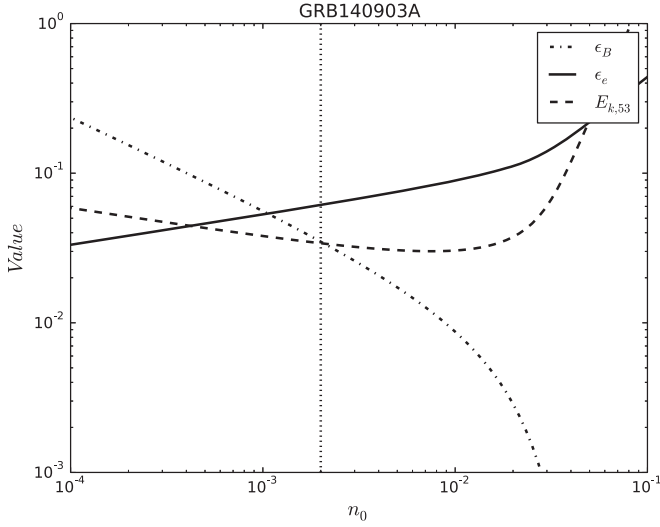


Figure 1. Numerical solutions of Equations (10)–(12) as functions of n_0 , assuming $\nu_c(t_d = 1) \sim 10$ keV. The vertical dotted line shows the location of $n_0 = 0.002$. The dotted-dashed, solid, and dashed lines represent the constraints on ϵ_B , ϵ_e , and E_k , respectively.

Equations (7)–(9) can be transferred to (Zhang et al. 2015)

$$\epsilon_{B,-2}^{1/2} E_{k,53} n_0^{1/2} \approx a, \quad (10)$$

$$E_{k,53} \epsilon_{B,-2}^{1/2} \epsilon_{e,-1}^2 \approx b, \quad (11)$$

$$E_{k,53}^{-1/2} \epsilon_{B,-2}^{-3/2} n_0^{-1} (1 + Y)^{-2} \approx c, \quad (12)$$

where

$$a = \frac{1}{6.6} \text{ mJy}^{-1} F_{\nu,\text{max}} D_{L,28.34}^2 \left(\frac{1+z}{2} \right)^{-1}, \quad (13)$$

$$b = \frac{1}{2.4} \times 10^{-16} \text{ Hz}^{-1} \nu_m C_p^{-2} \left(\frac{1+z}{2} \right)^{-1/2} t_{d,-3}^{3/2}, \quad (14)$$

$$c = \frac{1}{4.4} \times 10^{-16} \text{ Hz}^{-1} \nu_c \left(\frac{1+z}{2} \right)^{1/2} t_{d,-3}^{1/2}. \quad (15)$$

For observations, we know that $z = 0.351$, $p \approx 2.45$, $F_{\nu,\text{max}} \approx 180 \mu\text{Jy}$, $\nu_m(t_d = 2.5) = 37$ GHz (Troja et al. 2016), and $\nu_c(t_d = 1) \gtrsim 10$ keV. Thus we can solve Equations (10)–(12) numerically to obtain the values of ϵ_B , ϵ_e , and E_k as functions of n_0 , which are shown in Figure 1. Since we only know the lower-limit of ν_c , we can only obtain the upper-limit of ϵ_B and lower limits of ϵ_e and E_k for a fixed value of n_0 . For example, when $n_0 = 0.002$, we have $\epsilon_B \lesssim 0.03$, $\epsilon_e \gtrsim 0.06$ and $E_k \gtrsim 3.4 \times 10^{51}$ erg. Usually, $\max\{\epsilon_e, \epsilon_B\} \leq 1/3$ (the equipartition assumption) is required and we need $n_0 < 0.08$. Interestingly, this is in agreement with the expectation that the compact object mergers usually take place in lower density regions.

2.4. Numerical Fit to the Data

We fitted the multi-band afterglow numerically; the code was introduced in Fan & Piran (2006). If we do not consider the optical extinction, the radio, i band and X-ray data can be fitted well but r band is not acceptable (the reduced total chi-square is $\chi^2/\text{dof} \sim 3.05$ while r band contributes almost half of it); therefore, extinction must be considered. Troja et al. studied the afterglow spectral energy distribution of GRB

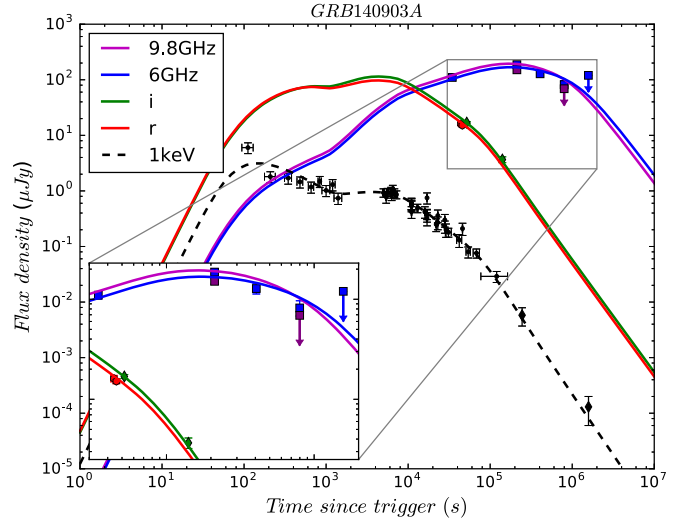


Figure 2. Fit of the multi-band afterglow light-curve. Black, red, green, blue, and purple represent X-ray (1 keV), r , i , 6 GHz, and 9.8 GHz bands respectively. The inset shows the fit of optical and radio observations.

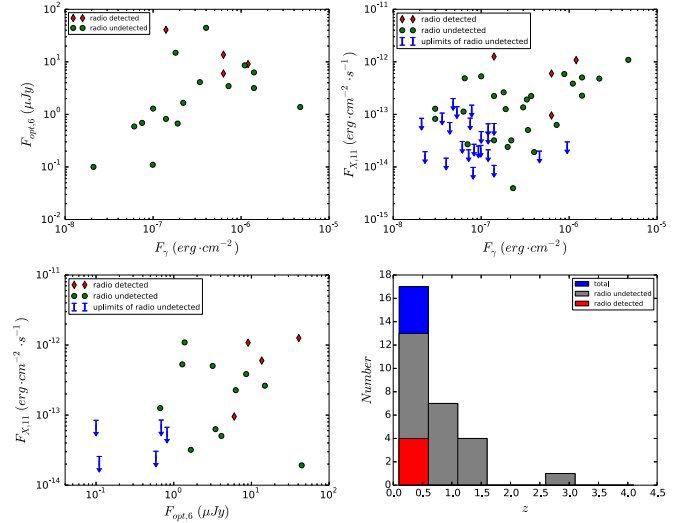


Figure 3. Upper left: relation between $F_{\text{opt},6}$ and F_γ . Upper right: relation between $F_{X,11}$ and F_γ . Lower left: relation between $F_{X,11}$ and $F_{\text{opt},6}$. Lower right: distribution of redshift. Optical and X bands flux densities are observed at 6 and 11 hr after bursts. Green dots and blue upper limits represent GRBs without radio afterglow detections and red dots represent GRBs with radio afterglow detections.

140903A and gave the Galactic extinction $E_{B-V} \approx 0.03$ and an intrinsic extinction $E_{B-V} \approx 0.15$ (Troja et al. 2016). Assuming the host extinction model is the same as the Galactic, we can get the optical extinction $A_r \approx 0.68$ and $A_i \approx 0.5$.

Considering this extinction, we can fit the radio, optical, and X-ray light curves well. We use the scenario of a normal expanding jet with a later energy injection. The numerical results are presented in Figure 2, we found that this set of fitting parameters (ϵ_e , ϵ_B , p , n_0 , $E_{k,51}$, θ_j , t_i , t_f , A) $\sim (0.06, 0.01, 2.45, 0.002, 5, 0.05, 1000, 7000, 6 \times 10^{48})$ can reasonably fit the data, where θ_j is the half-opening angle of the GRB outflow. Due to the lack of afterglow data in the early time, the only constraint on the initial Lorentz factor is $\Gamma_0 \geq 200$, and we took 200 in the fit. The values of $E_{k,51}$, t_i , t_f ,

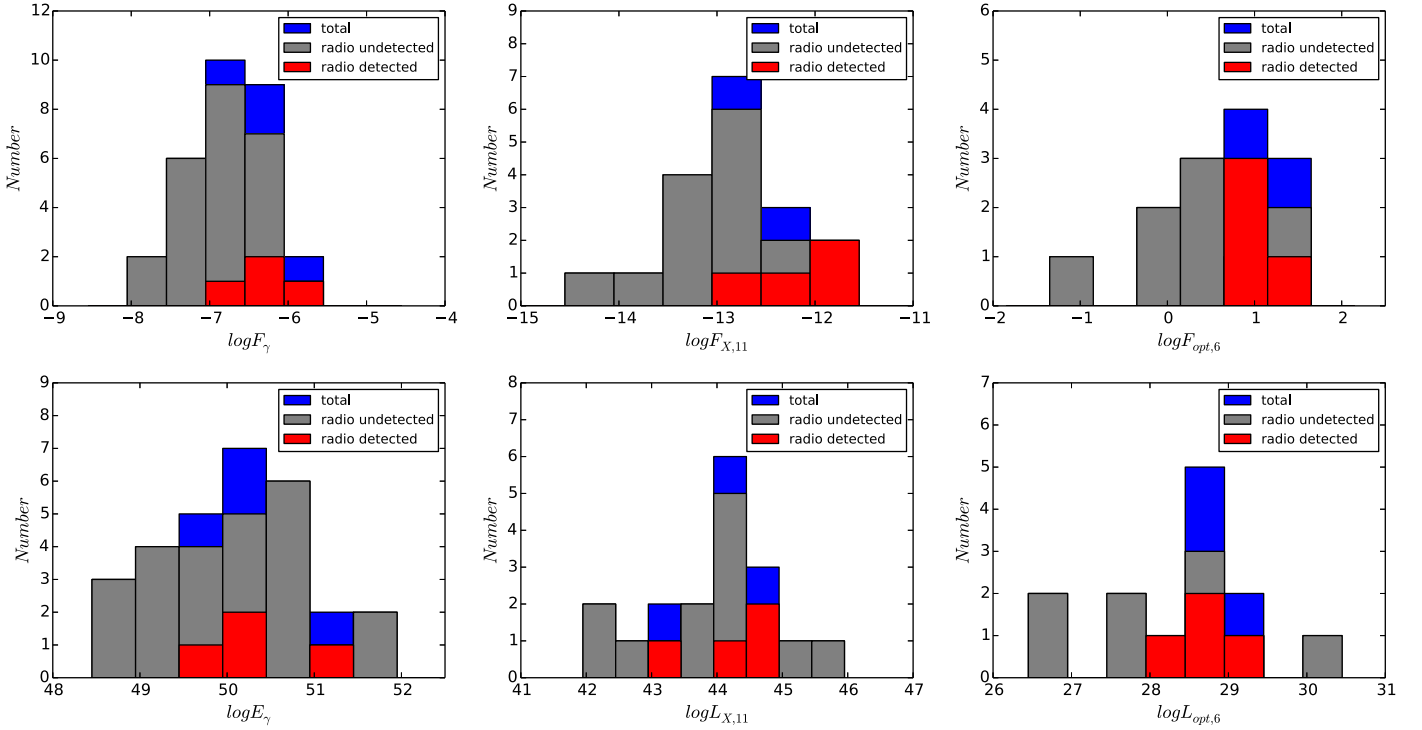


Figure 4. Distributions of F_γ , $F_{X,11}$, $F_{\text{opt},6}$ and E_γ , $L_{X,11}$, $L_{\text{opt},6}$. Red and gray colors represent samples of GRBs with and without radio afterglow detections and blue represents the total sample.

and A are consistent with previous analytical results. The reduced chi-square is $\chi^2/\text{dof} \sim 1.3$.

In our fit (see Figure 2), the X-ray afterglow first decays before 1×10^3 s and is followed by a continuous energy injection until 7×10^3 s. Then, it turns to a normal decay. At about 1×10^5 s, a jet break appears.

In previous work, Zhu et al. (2015) studied another short GRB 130912A, which also has a long-lasting optical plateau. However, in that case, the plateau phase can be explained without an energy injection. Here, GRB 140903A has a longer-lasting X-ray plateau and this could be explained by energy injection from 10^3 s to 7×10^3 s.

Troja et al. (2016) got a different set of physical parameters (ϵ_e , ϵ_B , n_0 , $E_{k,\text{iso}}$, θ_j) $\sim (0.14^{+0.19}_{-0.06}, 2.1^{+3.6}_{-1.4} \times 10^{-4}, 0.032^{+0.14}_{-0.026}, 4.3^{+1.2}_{-2.0} \times 10^{52}, 0.090 \pm 0.012 \text{ rad})$ and an observing angle of $\theta_{\text{obs}} \sim 0.055 \text{ rad}$. This is natural since we use the energy injection model, which is different from their off-axis jet model. We note that the difference in density may explain most of the differences in the physical parameters. However, one should note that in our energy injection model, the total kinetic energy at the end of energy injection is $\sim 4.1 \times 10^{52} \text{ erg}$, which is consistent with that of Troja et al. (2016).

3. STATISTICAL STUDY

Except GRB 140903A, there are only three SGRBs whose radio afterglows have been detected. The properties of those SGRBs have been summarized by Berger (2014). Although the sample is small, we can still do some primary statistics work for the purpose of finding the difference between SGRBs with and without radio afterglow detections.

Berger (2014) described a sample of 70 SGRB events with fluence measurements in 15–150 keV (F_γ); 28 (23) of the 70 events have fluxes of 0.3–10 keV, with measurements (upper

limits) at 11 hr postburst ($F_{X,11}$), and 28 of 70 events have measured redshifts (z).

Together with GRB 140903A, for which all of the F_γ (Palmer et al. 2014), $F_{X,11}$, and z (Cucchiara et al. 2014) have been measured, the total sample consists of 71 SGRB events. Of 71 events, 13 have optical afterglow (Fong et al. 2015) data that can be fitted by a broken power law. Then, we can get optical flux density at 6 hr postburst ($F_{\text{opt},6}$).

Figure 3 shows the relations between fluence and flux (densities) of different bands and the distribution of redshifts. We can see that in the three panels at the front, GRBs with radio afterglow detection generally locate in the upper right side, and in the last panel they all gather at the lower redshift region. This is natural since the “nearby” events are usually brighter and easier to detect (in radio and also other bands).

In order to compare the intrinsic properties of the SGRBs with and without radio afterglow detection, we compare the distributions of F_γ , $F_{X,11}$, $F_{\text{opt},6}$, and the corresponding energy (E_γ) and luminosity ($L_{X,11}$ and $L_{\text{opt},6}$) in Figure 4. Those SGRBs with radio afterglow detections have higher values of F_γ , $F_{X,11}$, $F_{\text{opt},6}$ but normal E_γ , $L_{X,11}$, and $L_{\text{opt},6}$. We also note that the radio observations are consistent with emission from the forward shock. This means that nearer and brighter SGRBs are more likely to have detectable radio afterglow emission. It is a natural consequence of the limited sensitivity of radio facilities and is consistent with the conclusion made by Chandra & Frail (2012) from long GRBs.

4. CONCLUSION

GRB 140903A is characterized by its $\sim 10^6$ s radio afterglow emission. Some optical and X-ray afterglow data have also been recorded, rendering GRB 140903A as one of the few short events with afterglow emission in a very wide energy

range (i.e., from radio to X-ray). We show in this work that the afterglow data can be self-consistently reproduced within the forward shock radiation scenario and at $t \leq 7 \times 10^3$ s an energy injection from the prolonged activity of the central engine is needed. The energy injection form suggests that the central engine is likely millisecond magnetar, similar to that needed for interpreting the X-ray flat segment of SGRB 051221A (Fan & Xu 2006). Such a result may suggest a relatively small total-gravitational-mass of the pre-merger binary system or a very hard equation of state of neutron stars that can yield the maximum gravitational mass $> 2.3\text{--}2.4 M_{\odot}$, this is because for the 10 neutron star binary systems observed in the Galaxy, their merger remnants will have a typical gravitational mass $\sim 2.3\text{--}2.4 M_{\odot}$, if no significant amount of material has been ejected (Fan et al. 2013). The inferred jet half-opening angle ~ 0.05 rad (2.9°) is very small, implying that hundreds more similar events took place in the local universe but in directions missing the Earth.

Relative to the “frequent” detection of SGRB afterglow in X-rays and optical, the radio afterglow emission had just been detected in four events. To better understand the rare detection in radio bands, we carry out a statistical study to see whether there is a significant difference between the events with and without radio detections. The common features of these radio-detected GRBs are the relatively small redshifts and higher flux or flux density especially in the optical band, implying that just the relatively nearby and energetic outflows are easier to give rise to detectable radio emission, consistent with the forward shock afterglow model.

We thank Dr. Y.Z. Fan for a stimulating discussion. This work was supported in part by 973 Programme of China under grant 2014CB845800, National Natural Science Foundation of China under grants 11273063, 11361140349, 11433009, 11303098, and 11103084, the Chinese Academy of Sciences via the Strategic Priority Research Program (grant No. XDB09000000) and the External Cooperation Program of BIC (No. 114332KYSB20160007).

REFERENCES

- Berger, E. 2014, *ARA&A*, **52**, 43
 Berger, E., Fong, W., & Chornock, R. 2013, *ApJL*, **774**, L23
 Berger, E., Price, P. A., Cenko, S. B., et al. 2005, *Natur*, **438**, 988

- Burrows, D. N., Grupe, D., Capalbi, M., et al. 2006, *ApJ*, **653**, 468
 Capone, J., Toy, V., Cenko, S. B., et al. 2014, GCN Circ, **16767**
 Cenko, S. B., & Perley, D. A. 2014, GCN Circ, **16770**
 Chandra, P., & Frail, D. A. 2012, *ApJ*, **746**, 156
 Cohen, E., & Piran, T. 1999, *ApJ*, **518**, 346
 Cucchiara, A., Cenko, S. B., Perley, D. A., Capone, J., & Toy, V. 2014, GCN Circ, **16774**
 Cummings, J. R., Burrows, D. N., Evans, P. A., et al. 2014, GCN Circ, **16763**
 Dai, Z. G., & Lu, T. 1998, *A&A*, **333**, L87
 De Pasquale, M., Maselli, A., & Cummings, J. R. 2014, GCN Circ, **16767**
 Dichiaro, S., Guidorzi, C., & Japelj, J. 2014, GCN Circ, **16781**
 Eichler, D., Livio, M., Piran, T., & Schramm, D. N. 1989, *Natur*, **340**, 126
 Fan, Y. Z., & Piran, T. 2006, *MNRAS*, **369**, 197
 Fan, Y.-Z., Wu, X.-F., & Wei, D.-M. 2013, *PhRvD*, **88**, 067304
 Fan, Y. Z., & Xu, D. 2006, *MNRAS*, **372**, L19
 Fong, W. 2014, GCN Circ, **16777**
 Fong, W., Berger, E., Margutti, R., & Zauderer, B. A. 2015, *ApJ*, **815**, 102
 Fong, W., Berger, E., Metzger, B. D., et al. 2014, *ApJ*, **780**, 118
 Fruchter, A. S. 2014, GCN Circ, **16776**
 Gunn, J. E., & Ostriker, J. P. 1969, *Natur*, **221**, 454
 Jin, Z. P., Hotokezaka, K., Li, X., et al. 2016, *NatCo*, **7**, 12898
 Jin, Z. P., Li, X., Cano, Z., et al. 2015, *ApJL*, **811**, L22
 Kasen, D., Badnell, N. R., & Barnes, J. 2013, *ApJ*, **774**, 25
 Kennea, J. A., & Cummings, J. R. 2014, GCN Circ, **16764**
 Kouveliotou, C., Meegan, C. A., Fishman, G. J., et al. 1993, *ApJL*, **413**, L101
 Levan, A. J., Cenko, S. B., Cucchiara, A., & Perley, D. A. 2014, GCN Circ, **16774**
 Li, L. X., & Paczyński, B. 1998, *ApJL*, **507**, L59
 Li, X., Hu, Y. M., Fan, Y. Z., & Wei, D. M. 2016, *ApJ*, **827**, 75
 Liang, E. W., Zhang, B. B., & Zhang, B. 2007, *ApJ*, **670**, 565
 Nayana, A. J., & Poonam, C. 2014, GCN Circ, **16815**
 Nousek, J. A., Kouveliotou, C., Grupe, D., et al. 2006, *ApJ*, **642**, 389
 Pacini, F. 1967, *Natur*, **216**, 567
 Palmer, D. M., Barthelmy, S. D., Baumgartner, W. H., et al. 2014, GCN Circ, **16768**
 Panaitescu, A. 2006, *MNRAS*, **367**, L42
 Panaitescu, A., Mészáros, P., Burrows, D., et al. 2006, *MNRAS*, **369**, 2059
 Piran, T. 1999, *PhR*, **314**, 575
 Sakamoto, T., Troja, E., Gehrels, N., et al. 2014, GCN Circ, **16813**
 Shapiro, S. L., & Teukolsky, S. A. 1983, Research Supported by the National Science Foundation (New York: Wiley)
 Soderberg, A. M., Berger, E., Kasliwal, M., et al. 2006, *ApJ*, **650**, 261
 Tanvir, N. R., Levan, A. J., Fruchter, A. S., et al. 2013, *Natur*, **500**, 547
 Troja, E., Sakamoto, T., Cenko, S. B., et al. 2016, *ApJ*, **827**, 102
 Woosley, S. E., & Bloom, J. S. 2006, *ARA&A*, **44**, 507
 Xu, D., Geier, S., Malesani, D., et al. 2014, GCN Circ, **16783**
 Yang, B., Jin, Z. P., Li, X., et al. 2015, *NatCo*, **6**, 7323
 Yost, S. A., Harrison, F. A., Sari, R., & Frail, D. A. 2003, *ApJ*, **597**, 459
 Zhang, B., Fan, Y. Z., Dyks, J., et al. 2006, *ApJ*, **642**, 354
 Zhang, B., & Mészáros, P. 2001, *ApJL*, **552**, L35
 Zhang, S., Jin, Z. P., & Wei, D. M. 2015, *ApJ*, **798**, 3
 Zhu, B., Zhang, F. W., Zhang, S., Jin, Z. P., & Wei, D. M. 2015, *A&A*, **576**, A71